Front-orography interactions during landfall of the New Year's Day Storm 1992

Clemens Spensberger[1,2] and Sebastian Schemm[2]

[1]Geophysical Institute, University of Bergen and Bjerknes Centre for Climate Research, Bergen, Norway
[2]Institute for Atmospheric and Climate Science, ETH Zurich, Zurich, Switzerland

Correspondence: C. Spensberger (clemens.spensberger@uib.no)

Abstract. Although following a common synoptic evolution for this region, the New Year's Day Storm 1992 was associated with some of the strongest winds observed along the Norwegian West Cost. The narrow wind band along its bent-back front became famous as the "poisonous tail", and paved the way towards today's sting jet terminology. This article re-examines the storm's landfall with a particular focus on the interaction with the orography.

Sensitivity analyses based on WRF simulations demonstrate that the formation and the evolution of the warm-air seclusion and its "poisonous tail" are largely independent from orography. In contrast, the warm sector of the storm is undergoing considerable orographically induced modifications. While moving over the orography, both warm and cold fronts are eroded rapidly. This development fits neither the cold-air-damming nor the passive-advection paradigms describing front-orography interactions. The warm sector is lifted over the orography, thereby accelerating the occlusion process. The insensitivity of the warm-air seclusion to the orographic modifications of the warm sector raises the question to which extent these entities are still interacting after the onset of the occlusion process.

Further, we observe ubiquitous and large-amplitude internal gravity waves (IGWs) during the landfall of the warm and cold fronts, exceeding in amplitude the cross-frontal circulation. As the spatial scales of the IGW pattern and of the fronts are comparable, wave-front interactions are plausible and might have contributed to the erosion of the cross-frontal temperature gradient over the orography. Further, we hypothesize that IGWs contribute to the observed near-instantaneous flow deflection around the orography at 500 hPa, which is well above crest height.

1 Introduction

The New Year's Day Storm 1992 (norw.: *Nyttårsorkanen*) was one of the most vigorous winter storms in the history of recorded storms over Norway. Its wind gusts exceeded the upper limits of measurement stations along the Norwegian West Coast. Through extrapolation, the Norwegian national weather service (MET Norway) estimated wind gusts exceeding $60\,\mathrm{m\,s^{-1}}$ and 10-min mean wind speeds exceeding $45\,\mathrm{m\,s^{-1}}$ at Svinøy lighthouse during the landfall (locations and orography shown in Fig.

1; Aune and Harstveit, 1992). Along the coastline from the Svinøy Lighthouse to the vicinity of Trondheim, the wind speeds are estimated to have had return periods of more than 200 years (Aune and Harstveit, 1992).

Consequently, the storm attracted the attention of the scientific community. In particular the formation of the extreme wind speeds along the bent-back front and the formation of a warm-air seclusion received attention (Grønås, 1995; Browning, 2004; Clark et al., 2005). With his study, Grønås (1995) introduced the "poisonous tail" as a widely-used metaphor to the scientific literature. The term "poisonous tail" was already used by the Norwegian forecasting community before the work of Grønås (1995), who learned about it while working as a forecaster at MET Norway in the 1960s. Later, Browning (2004) and Clark et al. (2005) turned the "poisonous tail" into the "sting at the end of the tail", which has become a term popular even in the media (Schultz and Browning, 2017). In his analysis of the New Year's Day Storm, Grønås (1995) found that moist diabatic processes played a crucial role in the formation and evolution of the warm-air seclusion. We complement his analysis, investigating the role of front-orography interactions in the evolution of the storm. Specifically, we investigate the role of the landfall on the Scandinavian coastal range (Scandes) in the formation and evolution of the warm-air seclusion, addressing the following questions:

1. Did the landfall of the storm affect the formation of its poisonous tail?
2. Did the landfall affect the track of the New Year's Day Storm?
3. How did the landfall affect the warm and cold fronts of the New Year's Day Storm?

To shed light on these questions, we contrast WRF simulations with double the Scandinavian orography and with no Scandinavian orography.

Previous case studies on front-orography interactions often focus only on cold fronts (e.g. Braun et al., 1997; Kljun et al., 2001; Neiman et al., 2004), although a limited number also consider bent-back fronts (e.g. Steenburgh and Mass, 1996) or warm fronts (e.g. Doyle and Bond, 2001). Together, these case studies document numerous processes that can be at play during front-orography interactions, for example front dissipation due to orographic flow deformation (Braun et al., 1997), the formation of barrier jets (Braun et al., 1999; Yang et al., 2017), front retardation due to blocking (Doyle and Bond, 2001; Neiman et al., 2004), as well as foehn and cyclogenesis in the lee (Kljun et al., 2001).

Due to the complexity of the front-orography interplay, only a limited number of conceptual models exist. One of the earliest efforts is presented by Bjerknes and Solberg (1921), who summarised rain observations over Scandinavia in a conceptual model of a warm front moving over a ridge. Their conceptual model includes a pocket of trapped cold air upstream of the ridge and a warm front modified by the vertical motion up- and downstream of the ridge. Davies (1984) and Egger (1992) apply the idea of orographically blocked flow to a non-linear analytical model of cold fronts approaching a triangular ridge. In their model, the approaching cold front is entirely blocked in a certain parameter regime, for example for strong stratification. In contrast, if the flow is less stratified, the approaching front might be linearly advected by flow over the ridge (Blumen and Gross, 1987; Blumen, 1992). Here the flow over the ridge causes a weakening of the front upstream, and a strengthening downstream. The antipodal conceptual models of Davies (1984) and Blumen and Gross (1987) provide the framework within which we will interpret our results.

This study is organised as follows. A description of the underlying data sets, model simulations and analysis methods (sec. 2) is followed by a detailed synoptic discussion of the event (sec. 3). In section 4 we investigate the impact of the Scandes on the storm and address the questions we raised. We close with our summary and conclusions (sec. 5).

2 Data and methods

We base our analysis on 3-hourly data from the Norwegian Reanalysis Archive (NORA10; Reistad et al., 2011) as well as on sensitivity experiments using the Weather Research and Forecasting model (WRF; Skamarock et al., 2008). The horizontal resolution of the NORA10 data set varies between 10 and 11 km, with the NORA10 orography and domain boundaries indicated in Fig. 1. In the vertical, the data is interpolated from 40 hybrid model levels to 25 pressure levels, covering the lower troposphere (1000–700 hPa) with a uniform resolution of 25 hPa, and a resolution of 50 hPa above.

2.1 WRF control and sensitivity simulations

The WRF model setup parallels that of the NORA10 hindcasts. We use a constant horizontal resolution of 10 km, but the WRF standard configuration with 60 hybrid model levels in the vertical. In both models the uppermost grid point is at 10 hPa, and the vertical resolution in the middle troposphere is about 35-40 hPa. The WRF output is interpolated to the same 25 pressure levels as the NORA10 data. The domain horizontally covers an area of 6000×4000 km, including most of the North Atlantic and of Scandinavia. The domain fully covers the region shown in Fig. 1. The Norwegian West Coast is located centrally in the eastern half of the model domain to minimise the impact of the model boundaries.

The initial state and boundary conditions are derived from 6-hourly ECMWF operational analyses. As the operational analyses for the study period do not include sea-surface temperature, we supplement with those from ERA-Interim (Dee et al., 2011). We initialise the model on 31 December 1991 06 UTC, roughly 21, 24, and 27 hours before the landfall of the warm, cold, and bent-back fronts, respectively. We chose this initialisation time as a trade off between having sufficient model spin-up time and the accuracy of the simulation. We tested initialisation dates between 30 December 1991 12 UTC and 31 December 1991 UTC and find that the earlier the initialisation date, the weaker becomes the simulated New Year's Day Storm.

We use WRF version 3.8.1 in a configuration with YSU boundary layer physics, the revised MM5 scheme (based on a Monin Obukhov surface layer with Carlson-Boland viscous sublayer), and the WRF three-class single moment cloud microphysics scheme. The parameterisation of cumulus convection is enabled, using the Kain-Fritsch scheme updated every 5 minutes. Radiation is calculated using the RRTM for long wave lengths, and the Dudhia scheme for short wave lengths, both updated every 10 minutes. The land surface is parameterised using a thermal diffusion model with five layers.

To test the sensitivity of the evolution of the New Year's Day Storm to the Scandinavian orography, we compare a simulation with full orography ("Control") to (a) a simulation in which the orography is removed and the land surface replaced by ocean ("Ocean"), and (b) a simulation in which we double the height of the Scandes ("Double"). In the Ocean simulation, sea-surface temperatures over the Scandinavian peninsula are defined by iteratively minimising the local Laplacian given the observed

surface temperatures in the surrounding seas (277-280 K in the Atlantic and North Sea ; 275-278 K in the Baltic; 273-275 K in the White Sea).

2.2 Front detection

For our analysis of the landfall, we require a front detection scheme to track and visualise the evolution of the fronts close to orography in the comparatively high-resolution NORA10 hindcasts and WRF simulations. There are different approaches for the automated detection of fronts, but all of them struggle to detect fronts in the vicinity of orography. Many of the difficulties arise from the need of higher derivatives to pinpoint the exact location of a front line (e.g. in Hewson, 1998; Jenkner et al., 2010; Berry et al., 2011). We therefore follow the approach of Spensberger and Sprenger (2018) and detect frontal volumes instead of front lines. Frontal volumes are defined as coherent volumes where the local thermodynamic gradient exceeds a given threshold

$$|\nabla\tau| > K\,, \tag{1}$$

and that exceed a given minimum volume. With this approach, we require only a first derivative of a thermodynamic field.

Spensberger and Sprenger (2018) developed this approach to detect fronts in the ERA-Interim data set. In our comparatively high-resolution data sets, mesoscale processes can lead to locally strong thermodynamic gradients independent from a synoptic-scale frontal system. We are however only interested in local thermodynamic gradients associated with a synoptic-scale front, and therefore require a minimum thermodynamic gradient both at the native resolution of the input data and in a smoothed version of the thermodynamic field. With this extension, we are able to identify only those mesoscale gradients that belong to a synoptic scale system, and define only those as fronts.

For the thermodynamic field τ, we use equivalent potential temperature θ_e to include both temperature and moisture gradients in the front definition [see Schemm et al. (2017) and Thomas and Schultz (2019) for a comprehensive discussion on the merits and drawbacks of θ_e for objective front detection]. We detect frontal volumes between 700 and 950 hPa with a minimum volume of $7500\,\mathrm{km}^2 \cdot 250\,\mathrm{hPa}$. Furthermore, we use a local $|\nabla\theta_e|$-threshold of $6.0\,\mathrm{K}\,(100\,\mathrm{km})^{-1}$ and a threshold for the smoothed field of $4.5\,\mathrm{K}\,(100\,\mathrm{km})^{-1}$. The conclusions of this study are independent from the exact values used for these thresholds.

To arrive at the lower-resolution data set, we smooth the θ_e field by 30 passes of a three-point filter $\tau_i^* = \tau_i + (\frac{1}{4}\tau_{i-1} - \frac{1}{2}\tau_i + \frac{1}{4}\tau_{i+1})$ in both horizontal dimensions. Here, i is the grid point index and $*$ denotes the new value after one pass of the filter. With 30 passes, this filter largely suppresses waves shorter than 10 grid points (approx. 110 km), while waves longer than approximately 20 grid points retain more than 50% of their amplitude.

3 Synoptic evolution during landfall

3.1 Explosive deepening over the central North Atlantic

We start following the synoptic evolution at 00 UTC on 1 January 1992, corresponding to 18 hours lead time of the WRF simulations (Fig. 2). At this point in time, the cyclone underwent an explosive deepening of approximately 40 hPa during the

preceding 24 hours (Grønås, 1995). Its structure is that of a mature cyclone following the Shapiro and Keyser (1990) conceptual model (Fig. 2a, b). The warm sector is bounded on the northern side by a well-developed bent-back front, and to the west by several cold front segments. On the warm front side, however, the θ_e gradient is below the detection threshold.

At this point in time, the strongest winds occur along the cold front (Fig. 3a), in agreement with, for example, the low-level jet described in Lackmann (2002). This low-level jet ahead of the cold front transports warm moist air towards the cyclone core, providing the inflow to a warm conveyor belt, as indicated by the broad area of stratiform ascent along the bent-back and warm fronts (vertical wind in Fig. 4a, b; cloud observations in Fig. 5). Although the absolute wind speed is smaller along the developing bent-back front than along the cold front jet, stronger ageostrophic winds indicate considerable flow imbalances along the developing bent-back front (exceeding $20\,\mathrm{m\,s^{-1}}$ in the NORA10 hindcasts; Fig. 3a). Parts of the wind speed difference between the bent-back and cold front might be due to the cyclone's direction of propagation: the winds along the cold front are largely parallel to this direction, whereas the flow along the bent-back front is largely opposing this direction.

3.2 Landfall of the warm sector

At 03 UTC on 1 January 1992, the leading edge of the warm sector arrives at the Scandes (Fig. 2c, d). At 850 hPa, the warm front does not fulfil our detection criteria except for a small region close to Svinøy on the northwestern cape of the West Coast, but at 925 hPa the temperature gradient exceeds the detection threshold in a line connecting Bergen with the cyclone's bent back front (not shown). The temperature gradient tightens as the front approaches the coast line, consistent with increased θ_e frontogenesis at 850 hPa driven by flow deformation (not shown). This flow deformation is consistent with an increase in ascent along the warm front as it approaches the Scandes (Fig. 4c, d).

The intensification of the fronts approaching the Scandes indicates some orographic blocking of the warm air mass that acts frontogenetically. The orographic flow distortion is associated with increasing ageostrophic wind components where the Scandes intersect with the 850 hPa surface (Fig. 3b). In contrast, at 700 hPa, parts of the warm sector already moved over the Scandes (not shown), which reach up to a crest height of about 850-800 hPa. Both the 700 hPa θ_e distribution and the corresponding cloud cover on the Meteosat 4 satellite imagery show hardly any orographic distortion (Fig. 5a), confirming that only levels below 850 hPa are affected by some degree of orographic blocking.

Between 03 and 06 UTC, the cold front crosses the North Sea and is at 06 UTC about to make landfall on the Norwegian West Coast (Fig. 2e, f). With the approaching cold front, the warm sector narrows to a thin filament along the coast line north of Bergen. To the south of Bergen, the Scandes are lower and the warm sector continues to propagate eastward relatively unaffected by the orography. This north-south difference in propagation speed further indicates that the warm front is partly blocked to the north of Bergen. At 850 hPa and below, the core of the cyclone is already largely cut off from the warm sector (Fig. 2e, f), while at 700 hPa core and warm sector remain connected (not shown).

During the landfall of the cold front, between 0430 UTC and 0600 UTC, satellite imagery shows the development of a cloud-free area on the eastern side of the Scandes (Fig. 5d). This cloud-free area indicates descending air masses and cloud evaporation. There is however some indication that this descent does not reach the lowest troposphere. First, the southwesterlies in the warm sector at 850 hPa are not evident in the wind field in the lee of the Scandes (Fig. 2e, f). Second, the 850 hPa

temperature in this region remains unchanged between 03 UTC and 06 UTC (Fig. 2c-f), suggesting that the lowest levels in the lee of the Scandes are at 06 UTC still covered by the incipient cold air mass.

Although some of the cold air moved over the Scandes after 09 UTC (Fig. 2g-j), the temperature gradient in the lee has become too diffuse to qualify as a cold front following our definition. Further, the previously clear signal in the vertical wind associated with the warm front (Figs. 4c,d) disappears over the Scandes. Over and in the lee of the Scandes, the vertical wind pattern is now dominated by wave structures indicating considerable activity of orographically triggered gravity waves (IGWs; Figs. 4c-h). These waves dominate over the organised vertical wind structure associated with the frontal circulation over the Atlantic and North Sea. The larger scale structure of the horizontal wind in the warm sector is re-emerging in the lee of the Scandes (compare Figs. 3b and 3d), although the peak wind speed is considerably reduced and features a superposed a wavy pattern consistent with IGWs. In contrast, over southern Sweden and Denmark, the cold front could propagate eastward without encountering any orography, leaving the wind structure largely intact (Figs. 3d).

3.3 Evolution of the warm-air seclusion

So far we focused the synoptic discussion on the landfall of the cold and warm fronts, and orographic impacts on the warm sector. In the following, we shift focus towards the remaining front structure, the bent-back front, and its evolution in tandem with the warm-air seclusion.

At 09 UTC, the warm-air seclusion is fully cut off from the warm sector at 850 hPa (Fig. 2g,h). The warm sector is located entirely on the eastern side of the Scandes, and covers the southern part of Scandinavia (Fig 2g,h). At 700 hPa, however, the warm-air seclusion is still largely connected with the warm sector, although the warm-air seclusion is now associated with a separate θ_e maximum close to the bent-back front (Fig. 6a). At 925 hPa, the Scandes separate the warm sector to the south from the warm-seclusion to the north (Fig. 6b).

With the formation of the warm-air seclusion, the cloud cover in the cyclone core starts to change. At 0300 UTC, the cyclone core is covered by low-level clouds, and partly even cloud-free. From 0430 UTC onward, the cyclone core is increasingly covered by spots of high-top convective clouds (Fig. 5c-e). The temporal correlation with the formation of the warm-air seclusion suggests that the onset of the convective activity in the cyclone core is dynamically linked with the cut-off of the seclusion from its warm sector. At 0730 UTC most of the warm-air seclusion is covered by patchy high clouds (Fig. 5e).

From 00 UTC to 09 UTC, the bent-back front continuously changes orientation. At 00 UTC the tip of the bent-back front points to the southwest, at 06 UTC to the south, and at 09 UTC to the southeast. The change of orientation is particularly pronounced between 06 UTC and 09 UTC, while the tip of the bent-back front is rapidly approaching the coast line. Between 09 UTC and 12 UTC, the bent-back front makes landfall and its orientation stops changing. Thus, the low-level jet associated with the bent-back front impinges on the coast line almost perpendicularly (Fig. 3d).

The following hours are characterised by a rapid decay of the warm-core seclusion (not shown). The weakening cyclone core crosses the Scandes between 15 and 18 UTC at around 65°N, where the Scandes are lower than further south. Together with the cyclone core, parts of the warm-air seclusion cross the Scandes, but in this process the temperature gradient along the bent-back front weakens, and no longer qualifies as a front following our definition.

3.4 Assessing the WRF Control simulation

Overall, WRF reproduces the synoptic evolution of the New Year's Day Storm well compared to the NORA10 reanalyses and the satellite imagery (Figs. 2, 4, 5). As indicated in the discussion of the synoptic evolution, there are however more or less subtle differences between NORA10 and WRF. Conceptually, the most prominent difference concerns the dynamics of the flow in the lee of the Scandes, between Svinøy and Trondheim at 06 and 09 UTC (blue circles in Fig. 4e,f). Here, WRF simulates a coherent region of descent which might be indicative of a foehn event, while the NORA10 hindcasts exhibit patchy up- and downdrafts indicative of convective activity.

In addition, the NORA10 hindcasts seem to lag behind both the satellite imagery and the WRF simulations. For example, the landfall of the cold front makes landfall on the Norwegian west coast around 06 UTC in NORA10 (Fig. 2e), compared to around 0430 UTC in the satellite imagery (Fig. 5c) and around 05 UTC in the WRF simulation (not shown). These and other differences between NORA10 and WRF are however inconsequential for the following discussion of orographic effects.

4 Orographic impacts

4.1 Little impact on the formation of the warm-air seclusion and its poisonous tail

In the synoptic evolution of the New Year's Day Storm in NORA10 and WRF, we observe a clear orographic influence on the storm. In particular, we found a separation of the cyclone core from its warm sector below 850 hPa, a synoptic evolution similar to the one described in Bjerknes and Solberg (1922). However, the extent to which the formation of the warm-air seclusion was forced or accelerated by the orography remains unclear. Levels above 850hPa did not experience an orographically forced cut-off of a pocket of warm air from the warm sector but still see a warm-air seclusion. To assess the impact of orography on the storm, we in the following compare simulations in which we either replaced the Scandinavian peninsula by ocean, or doubled the height of the Scandes.

These changes to the orography have surprisingly little impact on the evolution of the storm (Fig. 7). In particular, these simulations demonstrate that the warm-air seclusion would have formed even in the absence of orography (Fig. 7a). Without orography, the warm sector would have deformed to a long arched filament on 850 hPa (mark A in Fig. 7a), indicating an ongoing occlusion process independent from orography. The Scandes however accelerated this deforming and separation in an orographic occlusion process.

In tandem with the largely unaffected warm-air seclusion, the bent-back front shows hardly any orographic impact prior to its own landfall around 09 UTC (Fig. 7). In the Double simulation, the detected bent-back front extends less far around the warm-air seclusion than in the Ocean and Control simulations, indicating a less locally confined θ_e gradient on the northern side of the seclusion without orographic influence (Figs. 2h; 7). The structure of the wind field around the poisonous tail however are largely unaffected by the orography (not shown), and in particular unaffected by the landfall and decay of the storm's warm sector.

This insensitivity of the wind field might indicate that the extreme winds in the storm's poisonous tail are part of a sting jet, dynamically arising from downward transport of momentum (Schultz and Browning, 2017; Clark and Gray, 2018). However, in neither the NORA10 hindcasts nor our WRF simulations, there is a region of coherent descent that would indicate a sting jet (Fig. 4c-h). We therefore interpret the poisonous tail as predominantly a cold conveyor belt jet (Clark and Gray, 2018). In synthesis with the results of Grønås (1995), we suggest that the dynamics of the poisonous tail are more determined by local moist diabatic effects than the somewhat more remote orographic flow distortions.

In summary, the warm-air seclusion and its poisonous tail exhibit only weak sensitivity to the partial cut-off and rapid decay of the warm sector. This weak sensitivity suggests that the cyclone core and its warm sector hardly interact at this stage in the development. The fronts framing the warm sector decay quickly when moving over the Scandes and the warm conveyor belt inflow is at least partially interrupted. Yet, the warm-air seclusion evolves largely unaffected. Consequently, it might be most appropriate to regard the seclusion and the warm sector as two dynamically independent entities as soon as the occlusion process started. The evolution of these entities would then be in sync primarily because of a joint history rather than because of a persistent dynamical linkage.

The observation of Bjerknes and Solberg (1922) that secondary cyclogenesis frequently occurs at the occlusion point corroborates our interpretation. Cyclogenetic processes in the warm sector frequently lead to the formation of a secondary core rather than intensifying the incipient cyclone. Secondary cyclogenesis thus provides further indication that the dynamical ties between the warm sector and the incipient cyclone core tend to weaken considerably with the onset of the occlusion process.

4.2 Northward displacement of the warm-air seclusion

The main impact of the Scandes on the warm-air seclusion is a slight displacement to the north in the presence of orography that goes along with higher pressure on the upstream side of the Scandes. These orographically induced differences in the pressure (and hence mass) distribution are consistent with the orographically impacted mass transports in Figure 8. Figure 8 shows the mass transport σ at 850 hPa perpendicular to the geopotential isolines at this level. Here,

$$\sigma = -\rho \boldsymbol{v} \cdot \frac{\nabla \phi}{|\nabla \phi|} \quad , \tag{2}$$

where ρ is density, $\boldsymbol{v}$ the horizontal wind vector and ϕ geopotential.

Before landfall, mass transport towards the lower geopotential occurs primarily along the cold front (mark A) as well as a convergence line in the cold sector (mark B; Fig. 8a, b). Further, the mass transport exhibits a pronounced dipole structure around the cyclone core, which we expect mainly reflects the movement of the low pressure centre.

Even before the landfall of the fronts, the Scandes induce some mass transport towards lower pressure along the Norwegian west coast, peaking close to Svinøy (Fig. 8b). The mass transport peaks around 03 UTC (Fig. 8d), the time of the landfall of the warm front and the associated start of the orographic occlusion process. It is still a prominent feature of the mass transport around 06 UTC (Fig. 8f), when the orographic occlusion process completed the separation of the cyclone core from its warm sector. It is plausible that this orographically induced mass transport caused both the displacement of the cyclone core to the north, as well as the higher pressures along the Norwegian west coast.

Interestingly, this orographic mass transport is not restricted to the height of the orography. Although it is most pronounced below crest level, it remains visible throughout the troposphere, as for example at 500 hPa, shown in Figure 9. At this level, the orographic impact is evident in a dipole pattern centred over the Scandes in southern Norway that is consistent with a ridge evolving over the orography.

While the appearance of this orographically induced mass transport in the middle troposphere is hardly surprising, it might be instructive to ask what process causes its appearance. The 500 hPa mass transport evolves in tandem with the one at 850 hPa without discernible delay (shown for 03 UTC, compare Figs. 8d, 9b). Whatever does communicate the orographic impact to 500 hPa must hence do so rapidly.

4.3 Considerable impact on the warm and cold fronts

In order to investigate further, we follow the evolution of the warm and cold fronts in cross sections through the warm sector in the Ocean and Double simulations (Figs. 10, 11). Without orography, the cold sector catches up with the warm sector around 05 UTC, and an occlusion process begins (Fig. 10b). In this simulation ageostrophic winds exceeding $15\,\mathrm{m\,s^{-1}}$ occur solely in the boundary layer and along the eastward end of a wind maximum in the upper troposphere, around 400 km along the section in Fig. 10b.

In the Double simulation, the equivalent potential temperature and wind structure differs considerably from that in the Ocean simulation (Fig. 11). Most prominently, upstream of the Scandes a cold anomaly exceeding 8 K is evident both at 03 and 05 UTC. This cold anomaly indicates the orographically retarded propagation of the warm front at 03 UTC and a leftover pocket of incipient cold air trapped below 900 hPa at 05 UTC (Fig. 11a, b), similar to the one included the conceptual model of Bjerknes and Solberg (1921). Both at 03 UTC and at 05 UTC, low-level ageostrophic winds upstream of the Scandes exceed $35\,\mathrm{m\,s^{-1}}$. Throughout the shown evolution, wavy patterns in the ageostrophic wind component indicate IGW activity over the leeward slopes of the Scandes (Fig. 11). Consistent with this interpretation, these wavy patterns are even more pronounced in the stratosphere and there exceed amplitudes of 20 K in θ_e.

In the same region, isentropes are pulled down to follow the orographic slope over varying fractions of the troposphere (Fig. 11a-d). These simulated downdrafts are consistent with the appearing cloud-free area observed in the satellite imagery after the passing of the cold front (Fig. 5). Despite these downslope winds, neither the warm nor the cold sector affect the lowest level temperatures in the lee of the Scandes. This is particularly evident at 07 UTC, when the warm sector is located in the region between 800 km and 1000 km along the section in the Ocean simulation (Fig. 10c). In the same region, there is a pronounced cold anomaly below crest height in Figure 11c, showing that the orographically lifted warm sector hardly descends in the lee of the Scandes. This result confirms our previous interpretation of the orographic impact on the warm sector as an orographic occlusion.

A trajectory analysis based on the NORA10 hindcasts provides further support. Air parcels released in the North Sea upstream of the Norwegian west coast at 925 hPa in (a) the incipient cold air mass, (b) the warm sector and (c) the cold sector all are first lifted above the Scandes and then either level off or continue their ascent. Only few trajectories released in the cold sector descend the lee slopes of the Scandes. The warm sector is thus lifted off the surface in the lee of the Scandes.

With the flow moving predominantly over the Scandes, our case study differs considerably from previous case studies of cold and warm fronts impinging on the North American west coast (e.g. Braun et al., 1997; Doyle and Bond, 2001; Neiman et al., 2004) and of cold fronts impinging on the Alps (e.g. Kljun et al., 2001). All these case studies document larger degrees of orographic blocking and flow deviation around the orography. Consequently, the cold-air damming paradigm of Davies (1984) and idealised model of Egger and Hoinka (1992) provide little guidance to interpret our case study.

Although the flow is largely unblocked by the Scandes, the forced ascent over the orography interrupts the lowest part of the warm conveyor belt inflow towards the cyclone core. By cutting this link between the cyclone core (here, the warm-air seclusion) and its warm sector, the orographic impact on the New Year's Day Storm becomes an ideal natural experiment to clarify the dynamical relation between the cyclone core and its warm sector once the occlusion process has started. While the Scandes clearly affect the warm sector by retarding and eroding the fronts that move over the orography, the evolution of the warm-air seclusion is only slightly displaced to the north, but otherwise unaffected. This insensitivity of the core to the evolution of the warm sector suggests that the cyclone core at this stage of the life cycle has become a largely independent dynamical entity, that only co-evolves rather than interacts, with its warm sector. The observed tendency for secondary cyclogenesis at the occlusion point indicates that this finding for the New Year's Day Storm might apply more generally.

4.4 Potential role of IGWs

Finally, we can based on the presented evidence discuss potential dynamical mechanisms linking the Scandes with the induced a mass transport in the middle troposphere (Fig. 9). A most straightforward explanation would be that this signal arises through advection with the forced ascent on the upwind side of the Scandes. However, our trajectory analysis demonstrates that none of the parcels released at 03 UTC in the warm sector or at 06 UTC in the cold sector reach 500 hPa (Fig. 12d). Some parcels in the warm sector admittedly ascend to nearly 500 hPa, but their ascent to 550-600 hPa takes between 9 and 15 hours (Fig. 12d). This advective time scale is by far too long to explain the observed near-instantaneous adaptation of the 500 hPa flow, such that vertical ascent seems an implausible explanation.

A combination of hydrostatic and geostrophic adjustment might constitute a second potential causal chain linking the Scandes and the mid- and upper tropospheric flow. At the time of the anomalous mass flux in Figure 9, we observe a pronounced cold anomaly in the Double simulation compared to the Ocean simulation (Fig. 11a). Hydrostatic adjustment will rapidly communicate that signal upwards, lowering the geopotential in the column above. The following geostrophic adjustment is however inconsistent with the observed anomalous mass flux. First, the initial adjustment would constitute an acceleration towards the lowered geopotential, i.e. towards the Scandes, while the anomalous mass flux is directed along the coast line. Second, the geostrophically adjusted state would constitute an anomalous cyclonic circulation around the lowered geopotential. Along the coast line, this would imply a southward mass transport, which is the opposite of what we observe in Figure 9.

This leads us to hypothesize that the IGWs might have played a role in communicating the orographic flow distortion to the upper troposphere. We observed ubiquitous and high-amplitude IGW signatures in the vertical wind over and in the lee of the Scandes (Fig. 4). Through non-linear interactions, both between different waves and between a wave and the background state, IGWs can impart momentum on the background state (e.g. Einaudi et al., 1978; Plougonven and Zhang, 2014; Fritts et al.,

2016), plausibly leading to a deceleration in this case of orographically induced IGWs. In our case, the cross-frontal length scale of the approaching cold front is comparable to the wave length of the IGWs over the Scandes, such that wave-background state interactions seem plausible. A IGW-induced deceleration would in turn give rise to a geostrophic adjustment process with an initial acceleration towards the cyclone core, consistent with Figure 9.

Consistent with this hypothesis, IGWs might explain the rapid decay of in particular the cold front over the Scandes. The cross-front temperature contrast is considerably smoother in the lee of the Scandes (Fig. 2), and the vertical wind no longer shows any signs of the frontal circulation (Fig. 4e-h). This decay of the fronts is inconsistent with the conceptual model of Blumen and Gross (1987), in which the fronts are passively advected over an orographic obstacle to re-emerge with equal intensity in the lee.

5 Summary and conclusions

In summary, we followed the synoptic evolution of the New Year's Day Storm from its mature stage and through the landfall of, in sequence, the warm, cold and bent-back front. Based on our results and discussion, we now return to the questions we posed in the introduction.

- First, we find that the landfall of the storm hardly affected the formation of the warm-air seclusion and the storm's poisonous tail. This insensitivity is largely due to the cyclone's inherent occlusion process. The Scandes hence did not induce, but accelerate the occlusion process without considerably affecting the formation and evolution of the warm-air seclusion. Further, we find that the extreme wind speeds along the bent-back front of the storm, the poisonous tail, formed as a cold conveyor belt jet and would have occurred irrespective of orography. This insensitivity raises the question to which extent these the warm-core seclusion and the warm sector are still interacting after the onset of the occlusion process.

- Second, the landfall affected the track of the warm-air seclusion. The Scandes induced an anomalous mass flux along the Norwegian west coast towards the cyclone core which is most pronounced in the lowest troposphere, but extends up to the tropopause. The anomalous mass flux is consistent with the more northerly track of the storm in the presence of the orography.

- Third, the warm and cold fronts are strongly impacted by the landfall. While there is some indication of flow deviation around the orography and thus some degree of blocking, a trajectory analysis demonstrates that the flow was primarily moving over the Scandes. In this aspect, our case study deviates considerably from previous case studies in other regions which generally document a larger degree of blocking. For the same reason, the cold-air damming concept of Davies (1984) is not applicable to our case study. Neither, however, does our case study follow the Blumen and Gross (1987) paradigm of passive advection over the orography, because both the warm and cold front decay rapidly while moving over the Scandes. The rapid decay suggests interactions between the fronts and the orographically distorted flow.

Besides these questions, we describe two examples where internal gravity waves (IGWs) might have affected the synoptic evolution of the storm. First, they might have contributed to the orographically induced mass transport in the mid-troposphere that evolves in tandem with the low-level orographic flow distortion without discernible delay. Our trajectory shows that this mass transport emerges to rapidly to be explained by vertical advection. Further, the direction of the mass flux towards the cyclone core is consistent with a slow-down of the flow due to these orographic IGWs. Second, IGWs might have contributed to the erosion of the cold front while they passed over the Scandes. The cross-frontal length scale is comparable to the wave length, such that interactions are plausible. To underpin these more tentative results, and generalise them beyond the case study presented here, we require a more systematic assessment of the role of IGWs for front-orography interactions.

Author contributions. Both authors contributed to the analysis and writing of the manuscript.

Competing interests. We declare no competing interests.

Acknowledgements. We thank Thomas Spengler, Lukas Papritz, and Heini Wernli for interesting discussions, the Norwegian Meteorological Institute for providing the NORA10 reanalysis, the University Cooperation for Atmospheric Research (UCAR) for developing and providing the WRF model, the European Centre for Medium-Range Forecasts (ECMWF) for providing the boundary conditions used for the WRF simulations, and EUMETSAT for the Meteosat 4 imagery.

References

Aune, B. and Harstveit, K.: The Storm of January 1. 1992, Tech. Rep. 23/92 Klima, Det Norske Meteoroligiske Institutt, 1992.

Berry, G., Reeder, M. J., and Jakob, C.: A global climatology of atmospheric fronts, Geophysical Research Letters, 38, L04 809, https://doi.org/10.1029/2010GL046451, 2011.

Bjerknes, J. and Solberg, H.: Meteorological conditions for the formation of rain, Geofysiske Publikasjoner, II, 1–59, 1921.

Bjerknes, J. and Solberg, H.: Life cycle of cyclones and the polar front theory of atmospheric circulation, Geofysiske Publikasjoner, III, 1–16, 1922.

Blumen, W.: Propagation of fronts and frontogenesis versus frontolysis over orography, Meteorology and Atmospheric Physics, 48, 37–50–, https://doi.org/10.1007/BF01029558, 1992.

Blumen, W. and Gross, B. D.: Advection of a Passive Scalar over a Finite-Amplitude Ridge in a Stratified Rotating Atmosphere, Journal of the Atmospheric Sciences, 44, 1696–1705, https://doi.org/10.1175/1520-0469(1987)044<1696:AOAPSO>2.0.CO;2, 1987.

Braun, S. A., Houze Jr., R. A., and Smull, B. F.: Airborne Dual-Doppler Observations of an Intense Frontal System Approaching the Pacific Northwest Coast, Monthly Weather Review, 125, 3131–3156, https://doi.org/10.1175/1520-0493(1997)125<3131:ADDOOA>2.0.CO;2, 1997.

Braun, S. A., Rotunno, R., and Klemp, J. B.: Effects of Coastal Orography on Landfalling Cold Fronts. Part I: Dry, Inviscid Dynamics, Journal of the Atmospheric Sciences, 56, 517–533, https://doi.org/10.1175/1520-0469(1999)056<0517:eocool>2.0.co;2, 1999.

Browning, K. A.: The sting at the end of the tail: Damaging winds associated with extratropical cyclones, Quarterly Journal of the Royal Meteorological Society, 130, 375–399, https://doi.org/10.1256/qj.02.143, 2004.

Clark, P. A. and Gray, S. L.: Sting jets in extratropical cyclones: a review, Quarterly Journal of the Royal Meteorological Society, 144, 943–969, https://doi.org/10.1002/qj.3267, 2018.

Clark, P. A., Browning, K. A., and Wang, C.: The sting at the end of the tail: Model diagnostics of fine-scale three-dimensional structure of the cloud head, Quarterly Journal of the Royal Meteorological Society, 131, 2263–2292, https://doi.org/10.1256/qj.04.36, 2005.

Davies, H.: On the orographic retardation of a cold front, Beiträge zur Physik der Atmosphäre, 57, 409–418, 1984.

Dee, D. P., Uppala, S. M., Simmons, A. J., Berrisford, P., Poli, P., Kobayashi, S., Andrae, U., Balmaseda, M. A., Balsamo, G., Bauer, P., Bechtold, P., Beljaars, A. C. M., van de Berg, L., Bidlot, J., Bormann, N., Delsol, C., Dragani, R., Fuentes, M., Geer, A. J., Haimberger, L., Healy, S. B., Hersbach, H., Hólm, E. V., Isaksen, L., Kållberg, P., Köhler, M., Matricardi, M., McNally, A. P., Monge-Sanz, B. M., Morcrette, J.-J., Park, B.-K., Peubey, C., de Rosnay, P., Tavolato, C., Thépaut, J.-N., and Vitart, F.: The ERA-Interim reanalysis: configuration and performance of the data assimilation system, Quarterly Journal of the Royal Meteorological Society, 137, 553–597, https://doi.org/10.1002/qj.828, 2011.

Doyle, J. D. and Bond, N. A.: Research Aircraft Observations and Numerical Simulations of a Warm Front Approaching Vancouver Island, Monthly Weather Review, 129, 978–998, https://doi.org/10.1175/1520-0493(2001)129<0978:RAOANS>2.0.CO;2, 2001.

Egger, J.: The orographic deformation and retardation of a frontal zone, Meteorology and Atmospheric Physics, 48, 131–137, https://doi.org/10.1007/BF01029563, 1992.

Egger, J. and Hoinka, K.: Fronts and orography, Meteorology and Atmospheric Physics, 48, 3–36–, https://doi.org/10.1007/BF01029557, 1992.

Einaudi, F., Lalas, D. P., and Perona, G. E.: The role of gravity waves in tropospheric processes, pure and applied geophysics, 117, 627–663, https://doi.org/10.1007/BF00879972, 1978.

Fritts, D. C., Smith, R. B., Taylor, M. J., Doyle, J. D., Eckermann, S. D., Dörnbrack, A., Rapp, M., Williams, B. P., Pautet, P.-D., Bossert, K., Criddle, N. R., Reynolds, C. A., Reinecke, P. A., Uddstrom, M., Revell, M. J., Turner, R., Kaifler, B., Wagner, J. S., Mixa, T., Kruse, C. G., Nugent, A. D., Watson, C. D., Gisinger, S., Smith, S. M., Lieberman, R. S., Laughman, B., Moore, J. J., Brown, W. O., Haggerty, J. A., Rockwell, A., Stossmeister, G. J., Williams, S. F., Hernandez, G., Murphy, D. J., Klekociuk, A. R., Reid, I. M., and Ma, J.: The Deep Propagating Gravity Wave Experiment (DEEPWAVE): An Airborne and Ground-Based Exploration of Gravity Wave Propagation and Effects from Their Sources throughout the Lower and Middle Atmosphere, Bulletin of the American Meteorological Society, 97, 425–453, https://doi.org/10.1175/bams-d-14-00269.1, 2016.

Grønås, S.: The seclusion intensification of the New Year's Day Storm 1992, Tellus A, 47, 733–746, https://doi.org/10.1034/j.1600-0870.1995.00116.x, 1995.

Hewson, T. D.: Objective fronts, Meteorological Applications, 5, 37–65, https://doi.org/10.1017/S1350482798000553, 1998.

Jenkner, J., Sprenger, M., Schwenk, I., Schwierz, C., Dierer, S., and Leuenberger, D.: Detection and climatology of fronts in a high-resolution model reanalysis over the Alps, Meteorological Applications, 17, 1–18, https://doi.org/10.1002/met.142, 2010.

Kljun, N., Sprenger, M., and Schär, C.: Frontal modification and lee cyclogenesis in the Alps: A case study using the ALPEX reanalysis data set, Meteorology and Atmospheric Physics, 78, 89–105, https://doi.org/10.1007/s007030170008, 2001.

Lackmann, G. M.: Cold-Frontal Potential Vorticity Maxima, the Low-Level Jet, and Moisture Transport in Extratropical Cyclones, Monthly Weather Review, 130, 59–74, https://doi.org/10.1175/1520-0493(2002)130<0059:cfpvmt>2.0.co;2, 2002.

Neiman, P. J., Martin Ralph, F., Persson, P. O. G., White, A. B., Jorgensen, D. P., and Kingsmill, D. E.: Modification of Fronts and Precipitation by Coastal Blocking during an Intense Landfalling Winter Storm in Southern California: Observations during CALJET, Monthly Weather Review, 132, 242–273, https://doi.org/10.1175/1520-0493(2004)132<0242:MOFAPB>2.0.CO;2, 2004.

Plougonven, R. and Zhang, F.: Internal gravity waves from atmospheric jets and fronts, Reviews of Geophysics, 52, 33–76, https://doi.org/10.1002/2012RG000419, 2014.

Reistad, M., Breivik, Ø., Haakenstad, H., Aarnes, O. J., Furevik, B. R., and Bidlot, J.-R.: A high-resolution hindcast of wind and waves for the North Sea, the Norwegian Sea, and the Barents Sea, Journal of Geophysical Research: Oceans, 116, C05 019, https://doi.org/10.1029/2010JC006402, 2011.

Schemm, S., Sprenger, M., and Wernli, H.: When during their life cycle are extratropical cyclones attended by fronts?, Bulletin of the American Meteorological Society, https://doi.org/10.1175/bams-d-16-0261.1, 2017.

Schultz, D. M. and Browning, K. A.: What is a sting jet?, Weather, 72, 63–66, https://doi.org/10.1002/wea.2795, 2017.

Shapiro, M. A. and Keyser, D. A.: Extratropical Cyclones, Palmen Memorial Volume, vol. 182, book, microform Fronts, jet streams, and the tropopause, pp. 167–190, American Meteorological Society, 1990.

Skamarock, W. C., Klemp, J. B., Dudhia, J., Gill, D. O., Barker, D. M., Duda, M. G., Huang, X.-Y., Wang, W., and Powers, J. G.: A Description of the Advanced Research WRF Version 3, Tech. Rep. NCAR/TN-475+STR, NCAR Tech. Note, 2008.

Spensberger, C. and Sprenger, M.: Beyond cold and warm: an objective classification for maritime midlatitude fronts, Quarterly Journal of the Royal Meteorological Society, 144, 261–277, https://doi.org/10.1002/qj.3199, 2018.

Steenburgh, W. J. and Mass, C. F.: Interaction of an Intense Extratropical Cyclone with Coastal Orography, Monthly Weather Review, 124, 1329–1352, https://doi.org/10.1175/1520-0493(1996)124<1329:IOAIEC>2.0.CO;2, 1996.

Thomas, C. M. and Schultz, D. M.: What are the Best Thermodynamic Quantity and Function to Define a Front in Gridded Model Output?, Bulletin of the American Meteorological Society, 100, 873–895, https://doi.org/10.1175/bams-d-18-0137.1, 2019.

Yang, Y., Uddstrom, M., Revell, M., Moore, S., and Turner, R.: Damaging southerly winds caused by barrier jets in the Cook Strait and Wellington region of New Zealand, Monthly Weather Review, 145, 1203–1220, https://doi.org/10.1175/MWR-D-16-0159.1, 2017.

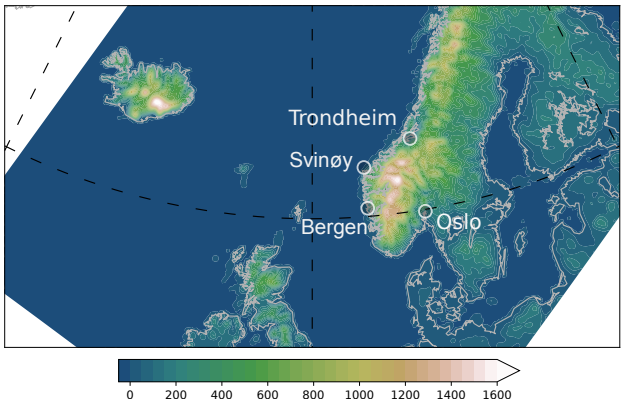

Figure 1. Orographic height map [m] from the NORA10 data set. The white circles show the location of some major cities and the Svinøy Lighthouse mentioned in the text.

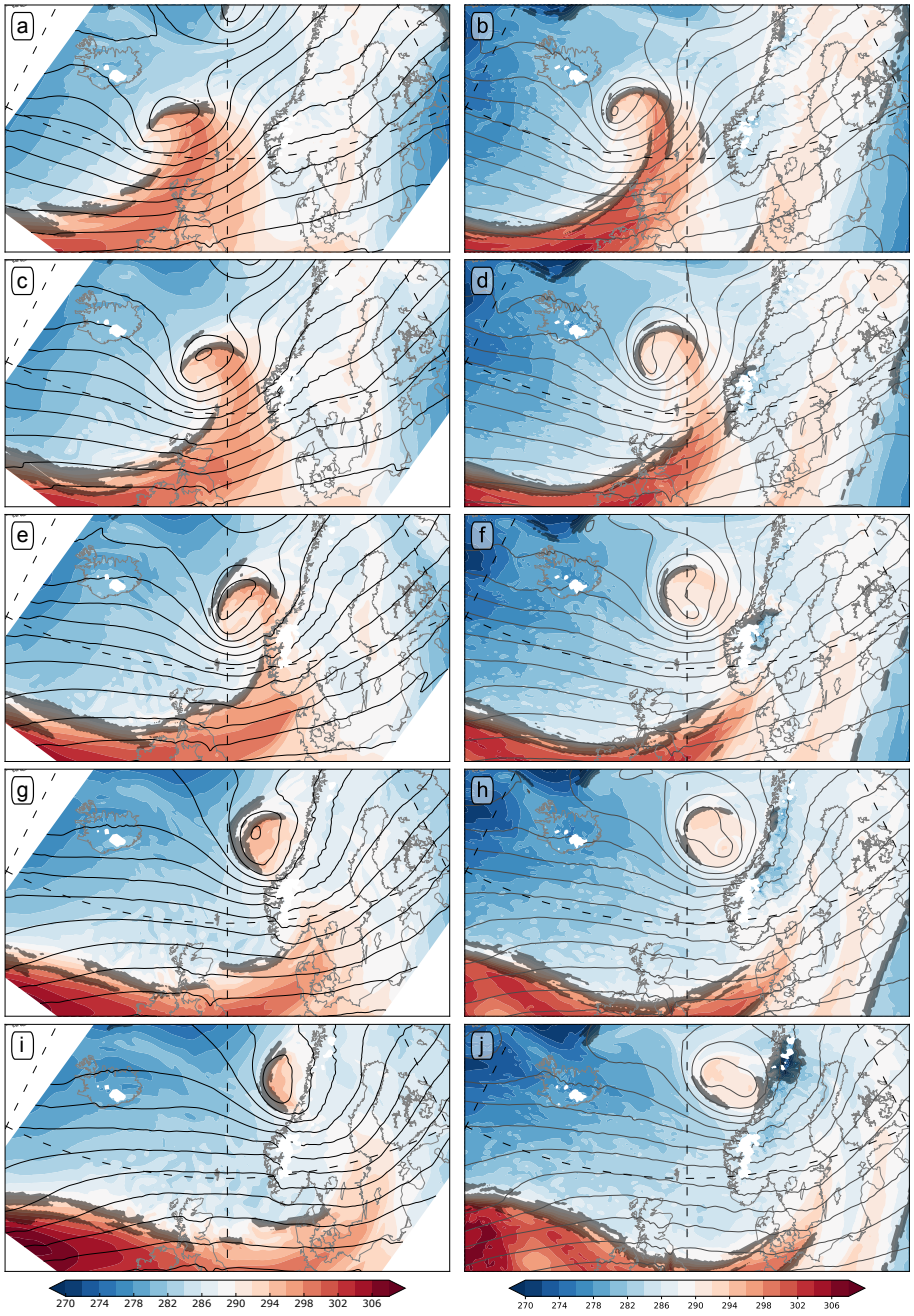

Figure 2. Frontal evolution for the New Year's Day Storm at 850 hPa. Equivalent potential temperature shading [K] and geopotential height contours with an interval of 50 m. Detected frontal zones are marked by dark shading. The panels show the development from (top row) 00 UTC through (bottom row) 12 UTC on 1 January 1992 in 3-hour intervals. The left column is based on the NORA10 hindcasts, the right on the Control simulation.

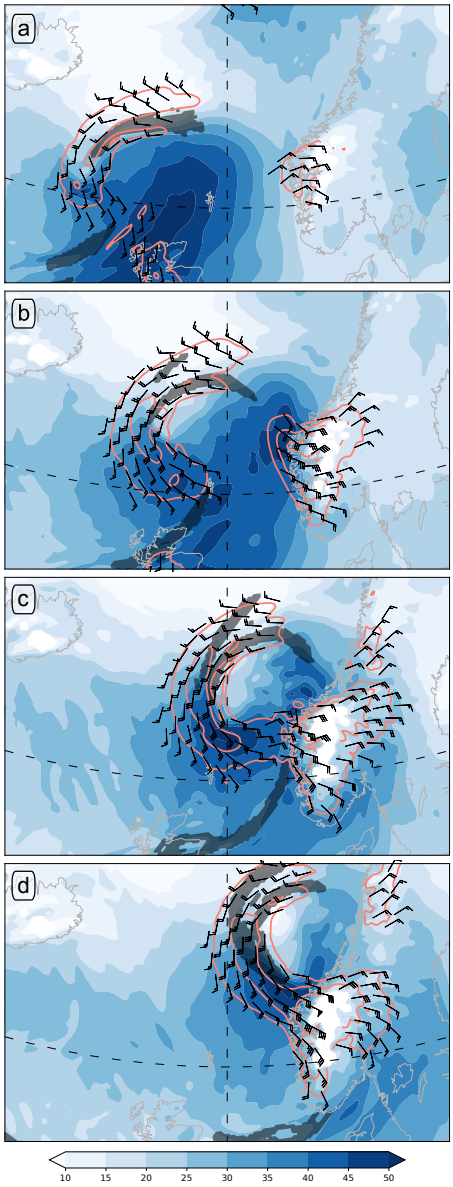

Figure 3. Full wind speed [$\mathrm{m\,s^{-1}}$] at 850 hPa in the NORA10 hindcasts on (a) 00 UTC, (b) 03 UTC, (c) 06 UTC and (d) 09 UTC of 1 January 1992. Barbs and pale red contours show ageostrophic wind with contours at 15, 25, and 35 $\mathrm{m\,s^{-1}}$. Dark shared regions show location of front volumes at 850 hPa as in Fig. 2.

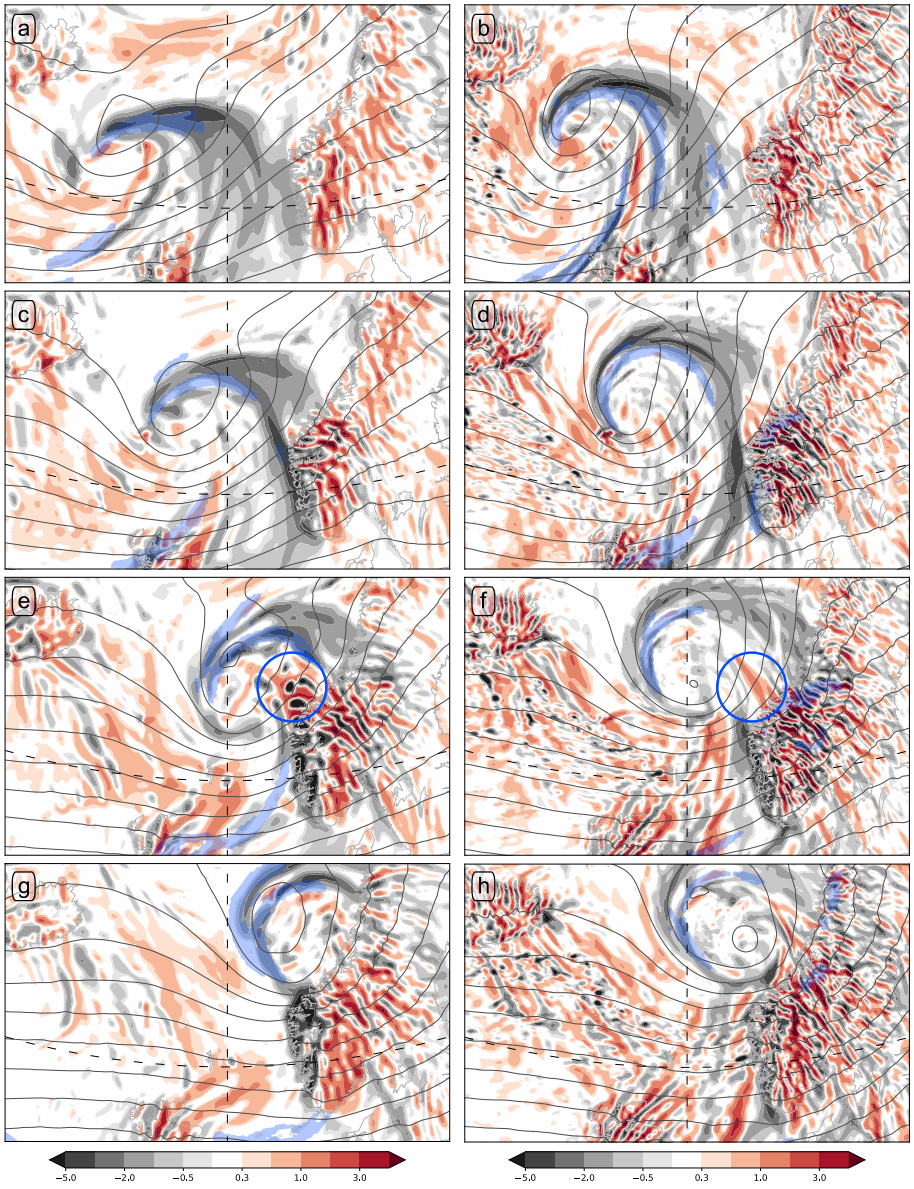

Figure 4. Pressure vertical velocity [Pa s^{-1}] at 700 hPa for (a,b) 00 UTC, (c,d) 03 UTC, (e,f) 06 UTC, and (g,h) 09 UTC. Dark grey contours show geopotential at 700 hPa, with a contour interval of 50 m, respectively. Blue shaded regions indicate the location of frontal zones at 850 hPa for both columns. The left column is based on the NORA10 hindcasts, the right on the Control simulation. For the blue circles in (e,f) refer to the main text.

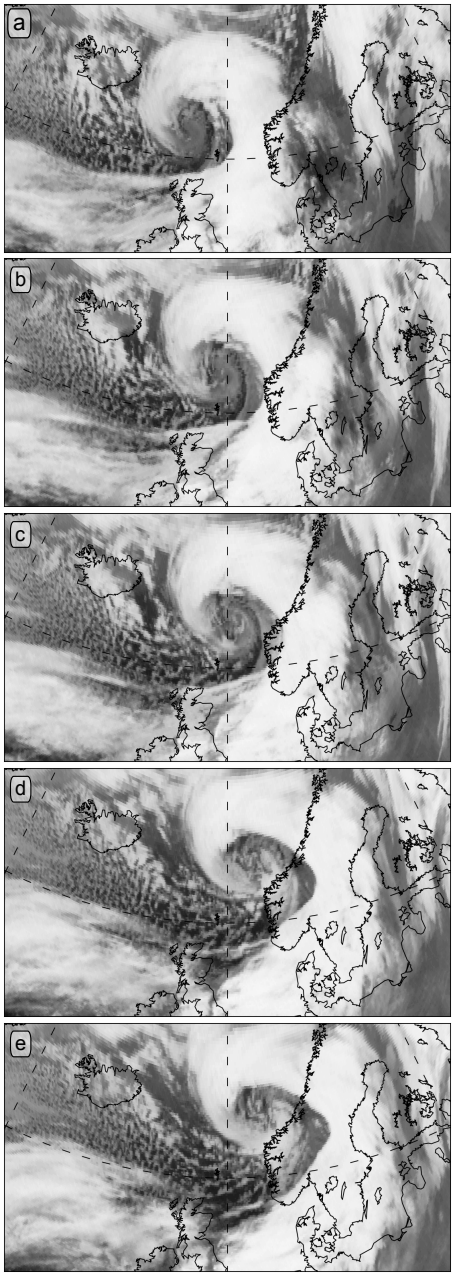

Figure 5. Remapped infrared imagery (10.8μm wave length, in $\mathrm{W\,m^{-2}\,sr^{-1}}$) from Meteosat 4 covering the landfall of the New Year's Day Storm from (a) 0130 UTC through (e) 0730 UTC on 1 January 1992 in 1.5-hour intervals. Imagery © EUMETSAT 2016.

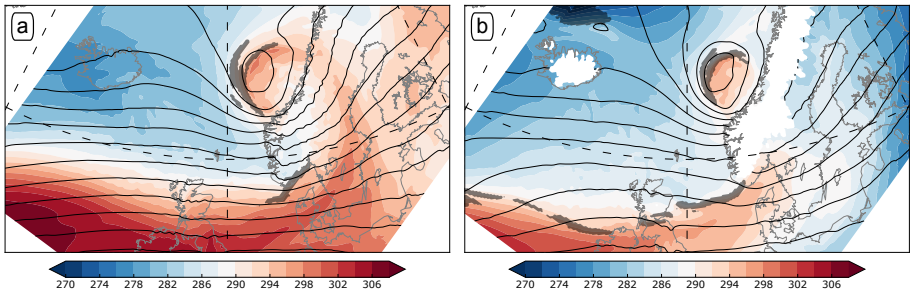

Figure 6. As Fig. 2g, but for (a) 700 hPa and (b) 925 hPa.

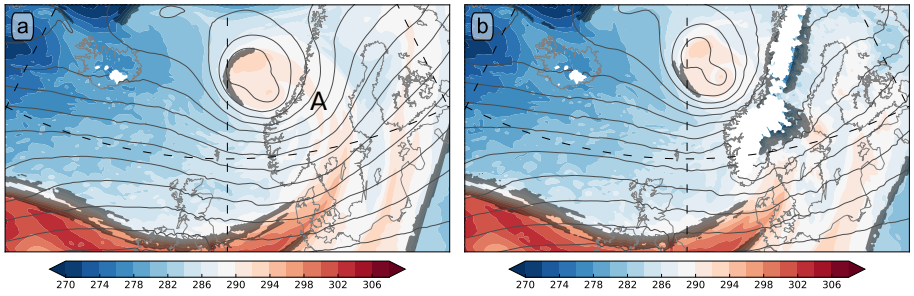

Figure 7. As Fig. 2h, but for (a) the Ocean simulation, and (b) the Double simulation. For the mark A, refer to the main text.

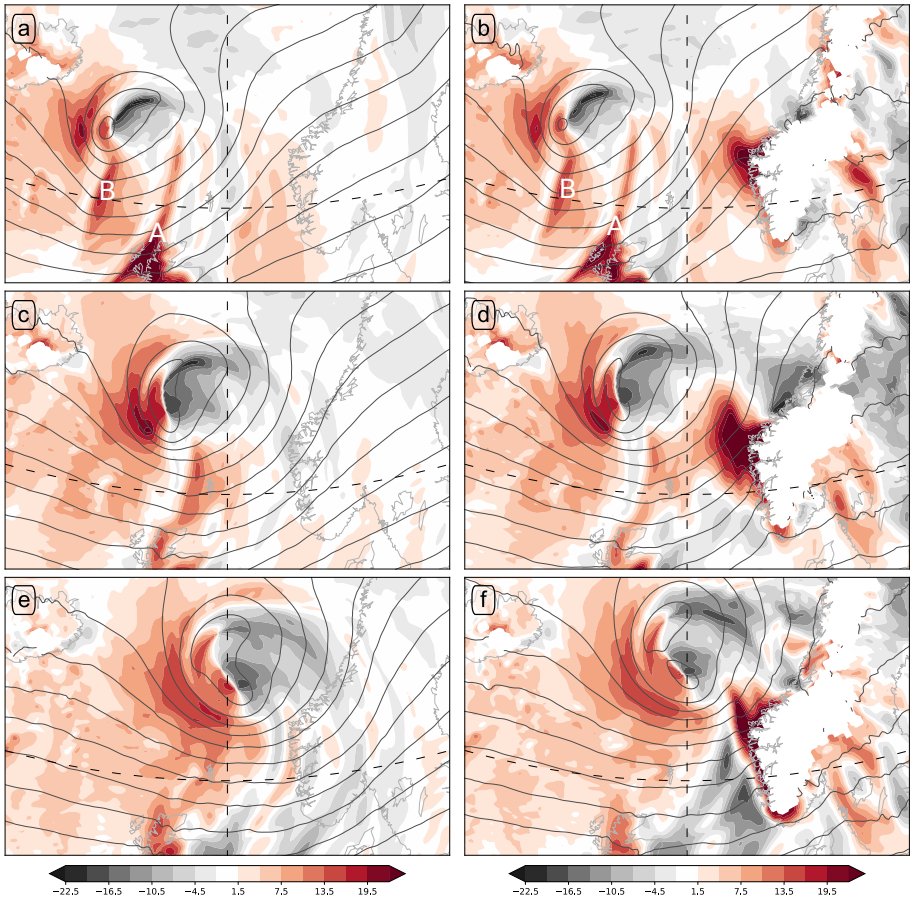

Figure 8. Mass transport [$\mathrm{kg\,s^{-1}\,m^{-2}}$] perpendicular to geopotential isolines at 850 hPa, with positive values indicating transport towards lower geopotential. The rows show the time evolution for (a,b) 00 UTC, (c,d) 03 UTC and (e,f) 06 UTC. The left column is based on a WRF simulation in which the Scandinavian orography as been removed and converted to ocean, the right column on a WRF simulation in which the Scandinavian orography is twice its original height. For the marks A, B refer to the main text.

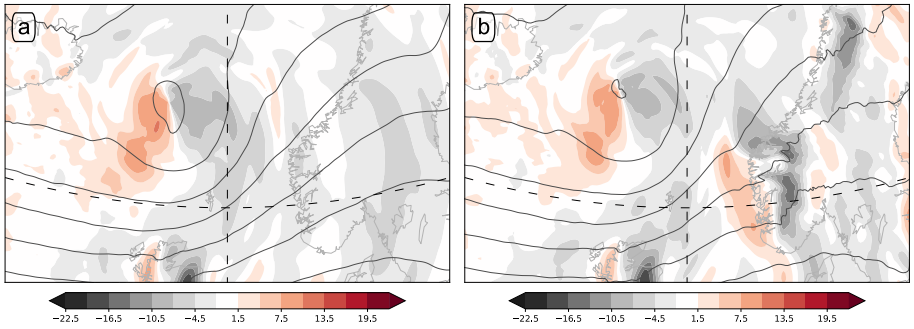

Figure 9. As Fig. 8c,d, but for mass transport at 500 hPa.

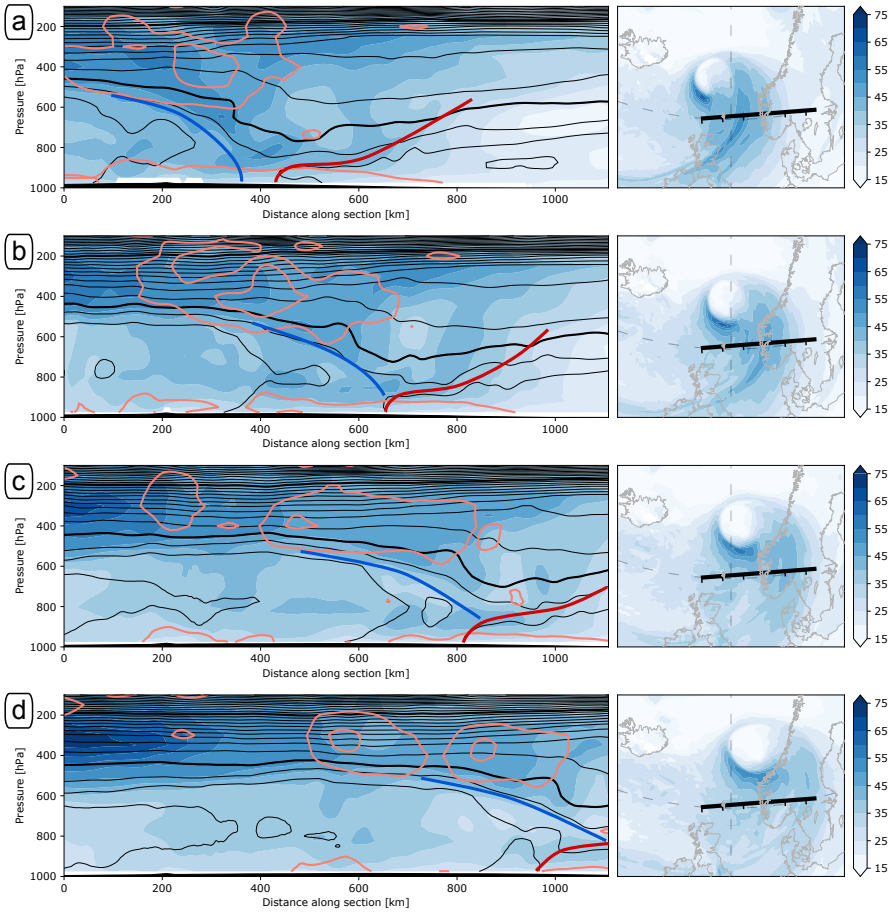

Figure 10. Cross section of wind speed (shading, $\mathrm{m\,s^{-1}}$), equivalent potential temperature (black contours with interval 5 K, 300,K and 350 K thickened) and ageostrophic horizontal wind with contours at 15, 25 and 35 $\mathrm{m\,s^{-1}}$. The blue and red lines mark subjectively analysed cold and warm fronts, respectively. The maps in the right column show wind speed at 850 hPa as well as the location of the cross section with ticks every 200 km. The rows show (a) 03 UTC, (b) 05 UTC, (c) 07 UTC, and (d) 09 UTC on 1 January 1992 for the Ocean simulation.

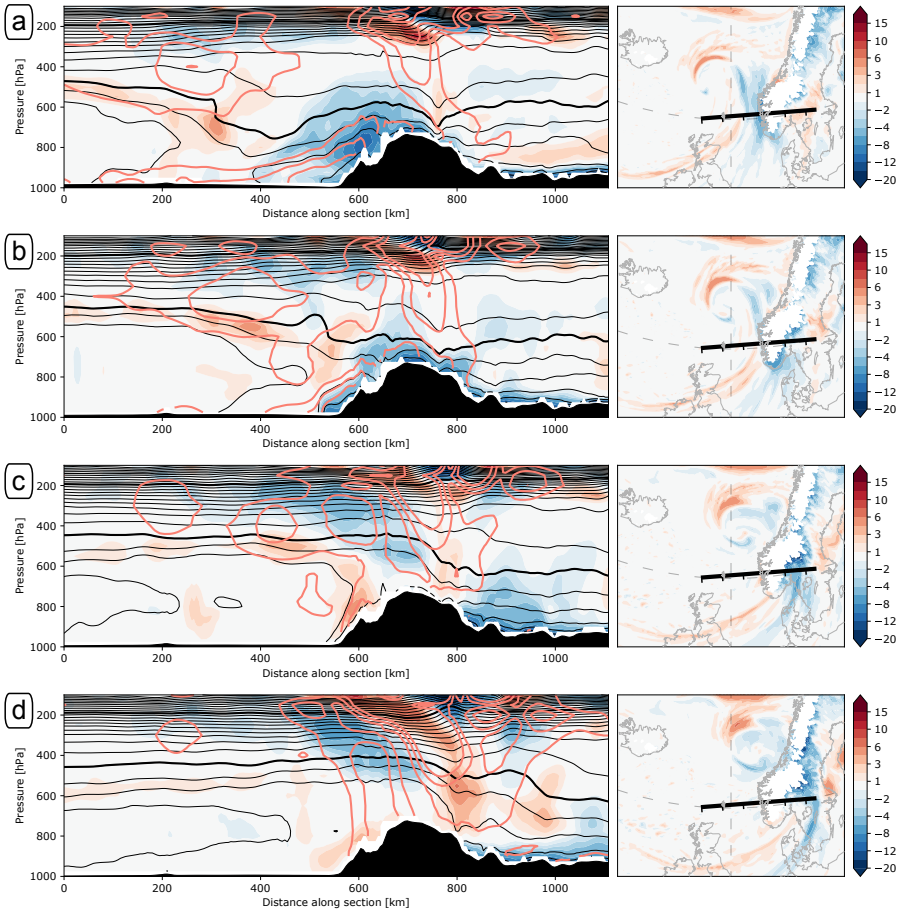

Figure 11. As Fig. 10, but showing in shading the equivalent potential temperature difference in Kelvin between the Double and the Ocean simulation in both the section and the map. Contours show equivalent potential temperature and ageostrophic wind speed as in Fig. 10, but for the Double simulation.

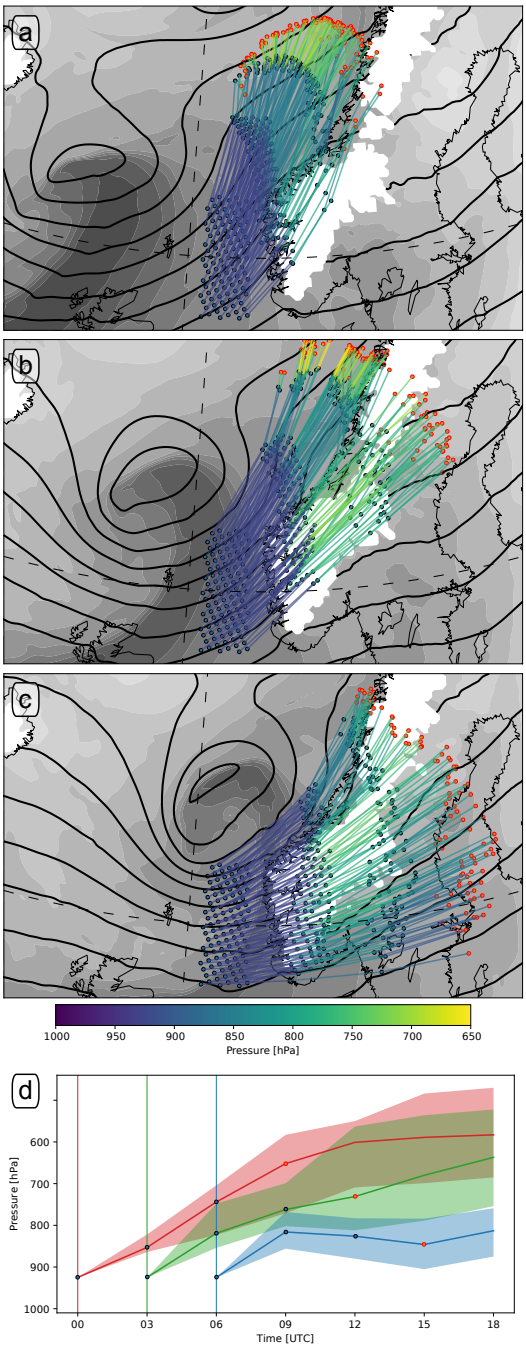

Figure 12. Forward trajectories released from the box 58.0-62.0°N, 1.0-4.0°E at 925 hPa at (a) 00 UTC, (b) 03 UTC and (c) 06 UTC. The trajectory segments between the circles each cover 3 hours, and they are coloured by pressure [hPa] of the *preceding* time step. The position of the parcels 9 hours after the respective release are red. The grey shading and black contours show θ_e and geopotential, both at 925 hPa, at the release time of the trajectories with the same contour interval and limits as in Fig. 2. Panel (d) shows the median pressure evolution of the above parcels. Circles indicate time steps shown in the trajectory maps (a)-(c). The respective transparent shading indicates variability between the trajectories by the 15 and 85 percentiles.